

¹Naval Research Laboratory, Monterey, CA, USA

²National Center for Atmospheric Research/NOAA/ERL Environmental Technology Laboratory, Boulder, CO, USA

A multi-scale simulation of an extreme downslope windstorm over complex topography

J. D. Doyle¹ and M. A. Shapiro²

With 16 Figures

Received September 29, 1999

Revised December 30, 1999

Summary

A severe localized windstorm, with near-surface winds $>60 \text{ ms}^{-1}$, occurred in an isolated valley within the Alpine mountains ($>1800 \text{ m}$) of central Norway on 31 January 1995. A multi-scale numerical simulation of the event was performed with the Naval Research Laboratory (NRL)'s Coupled Ocean/Atmosphere Mesoscale Prediction System (COAMPS), configured with four nested grids telescoping down to 1-km horizontal resolution. The windstorm occurred in response to topographic blocking and deformation of a lower-tropospheric warm front and attendant jet ($>35 \text{ ms}^{-1}$ at 2 km). The key findings are: i) mountain wave resonance and amplification arising from the interaction of the surface-based front and jet with complex orography, ii) sensitivity of the wave response to differential diabatic heating (vertical) gradients above the front, and iii) trapped response within the layer of large frontal stratification in the lower troposphere and subsequent amplification consistent with the theoretically-established two-layer windstorm analogue of Durran (1986).

1. Introduction

The unique topography of Norway, with its numerous deep fjords flanked by steep mountains, dramatically impacts local mesoscale weather events such as the windstorms that frequently occur in the vicinity of the complex topography surrounding the Norwegian Oppdal Valley. The valley, and its winter sports village of Oppdal, is located $\sim 80 \text{ km}$ from the west coast of Norway,

southwest of Trondheim, and north of the highlands of Jotunheimen and Dovre (Fig. 1). The occurrence of high wind events near Oppdal is quite common; a total of five destructive windstorms occurred during 1995 alone. This naturally raises questions regarding the origin of this local topographic forcing. On 31 January 1995, a high-wind event with gusts estimated $>60 \text{ ms}^{-1}$, caused substantial damage throughout the valley (Harstveit et al., 1995). This study examines the synergy between a topographically deformed front and a subsequent downslope windstorm using the Naval Research Laboratory's (NRL) high-resolution nonhydrostatic mesoscale modelling system. The evolution and dynamics of severe downslope windstorms associated with orographically-deformed fronts over three-dimensional complex topography remain somewhat of an enigma.

Numerical simulations of the 31 January 1995 windstorm were initially pursued to assess the ability of a sophisticated nonhydrostatic numerical model to capture the evolution of a severe windstorm amidst complex three-dimensional topography. On closer examination of the simulated event, a number of important issues became apparent regarding orographically forced windstorms in three dimensions in the presence of a complex environmental state. A further motivating factor is that this case, which features

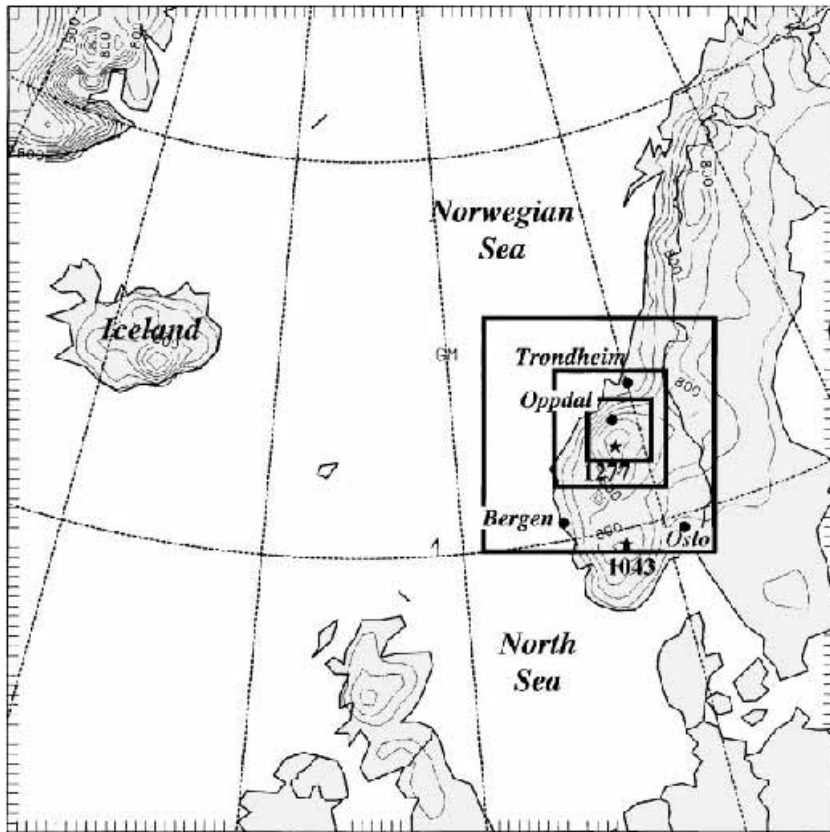


Fig. 1. Numerical model computational domain, coarse-mesh terrain field (200-m interval), and geographical locations of interest. The grid increments for the four nested meshes are 27 km, 9 km, 3 km, and 1 km, respectively

shallow mountain wave amplification over three-dimensionally complex topography, represents a significant departure from the classical windstorm situation in the vicinity of the Front Range of the U.S. Colorado Rocky Mountains (e.g., Lilly and Zipser, 1972; Lilly, 1978), which is often typified by deep (tropospheric/lower stratospheric) quasi-two-dimensional wave amplification. The specific objectives of the study are to

- i) evaluate the ability of a nonhydrostatic model to simulate the mesoscale characteristics of a downslope windstorm in three dimensions,
- ii) examine the structure and dynamics of a frontal zone as it impinges upon steep topography, and
- iii) explore the implications of frontal condensation and latent heat release on the windstorm dynamics.

Section 2 presents a theoretical overview of the problem. Section 3 contains the model description. The synoptic-scale and frontal-scale situation is discussed in Sect. 4. Section 5 describes

the fine-scale structure of the windstorm followed by the concluding remarks in Sect. 6.

2. Theoretical and observational overview

It is generally accepted that downslope windstorms are a manifestation of internal gravity wave amplification induced by air flow over an obstacle. The characteristics of downslope windstorms have been studied primarily along the eastern slope of the Colorado Front Range of the Rocky Mountains, coincident with the large population density of atmospheric scientists. Similar high-wind events occur along mountain lees such as in the Alps (Hoinka, 1985), Andes (Sarker and Calheiros, 1974), Cascades (Colle and Mass, 1998a), Dinaric Alps (Smith, 1987), Pyrenees (Campins et al., 1995), Rockies (Lilly and Zipser, 1972), and Sierra Nevada (Alka, 1960). The strongest events along the Rockies are characterized by peak gusts $> 50 \text{ ms}^{-1}$ that include distinct periodic wind-speed pulsations (Neiman et al., 1988; Scinocca and Peltier, 1989; Clark and Farley, 1984) and produce significant

structural damage (Lilly and Zipser, 1972). One particularly extreme example is the 11 January 1972 Front Range windstorm for which research aircraft observations suggested that the mesoscale structure was dominated by a large-amplitude quasi-hydrostatic wave (Lilly, 1978). Nearly the entire upstream flow was found to be subsiding into a ~ 2 km tropospheric layer. However, the Adriatic bora (Smith, 1987) and the Alpine foehn (Hoinka, 1985) have general similarities with the Colorado Front Range windstorms including internal hydraulic behavior. It is not generally known whether the quasi-two-dimensional characteristics are representative of downslope windstorms in the lee of other more complex terrain. For example, in regions of complex three-dimensional topography, gap and mountain wave dynamics may both contribute to the generation of strong low-level winds (Colle and Mass, 1998a).

Several distinct theories have been advanced to explain the origin of severe downslope windstorms as reviewed by Durran (1990). It should be noted that these theoretical treatments are almost exclusively two-dimensional. Eliassen and Palm (1960) theorized that upward propagating linear gravity waves are partially reflected by a layer containing strong vertical gradients in wind velocity and/or thermal stratification. Klemp and Lilly (1975) used linear perturbation theory to investigate the resonant response of hydrostatic waves in a multi-layer atmosphere. They hypothesized that gravity wave amplification is related to the partial reflection of upward propagating wave energy by static stability variations at various interfaces resulting in an optimal wave resonance or superpositioning. When the tropopause is located one-half vertical wavelength above the ground, the background state may be optimally tuned for maximum response.

Long (1953) theoretically addressed the similarity between downslope windstorms and hydraulic jumps. Applying this hydraulic perspective, Durran (1986) proposed that an increase in the velocity and decrease in the isentropic layer thickness, as the fluid ascends toward the mountain peak, lead to a subcritical to supercritical transition near the peak. The supercritical flow accelerates along the lee slope and eventually evolves to a turbulent hydraulic jump

as the flow returns to the downstream ambient conditions. This transcritical flow can be sensitive to the height of an elevated inversion with enhanced low-level stability providing a favorable environment for supercritical flow and large downslope windspeeds (Smith, 1985; Durran, 1986). The two-dimensional analytic solution to Long's equation for a single fluid layer with uniform stability and winds indicates that wave breaking will occur when the nondimensional mountain height, $\hat{h} = Nh_m/U$ (where N is the Brunt-Väisälä frequency, U is the mountain normal wind speed, and h_m is the obstacle height), exceeds 0.85 (Miles and Huppert, 1969). Solutions to Long's equation indicate that wave amplification occurs when a critical layer is present at $1/4 + n$ and $3/4 + n$ vertical wavelengths above the obstacle (Smith, 1985; Klemp and Durran, 1987). A limitation of the hydraulic analog is that the free surface assumption prevents vertical gravity wave propagation. However, the fundamental dynamics of windstorm conditions appear to be captured by internal hydraulic theory (Smith, 1985; Durran, 1986, 1992).

Nonlinear numerical simulations suggest that vertically propagating waves may become statically unstable and overturn above the tropopause prior to acceleration along the lee-slope (e.g., Clark and Peltier, 1977; Peltier and Clark, 1979). The wave-breaking region, which contains strong vertical mixing and local cross-mountain flow reversal, acts as a "wave- or self-induced critical layer" and reflects vertically propagating waves downward. Peltier and Clark applied linear theory to show that under certain conditions, the mountain wave becomes trapped between the level of overturning and the surface, and a resonant wave amplification occurs, resulting in strong surface lee-slope winds. The presence of an environmental critical level may intensify downslope winds (Colle and Mass, 1998b).

Strong downslope winds may occur when fronts interact with steep topography, in part because of the large static stability within the frontal inversions just above the mountain, and significant cross-barrier flow (e.g., Durran, 1990). Bjerknes and Solberg (1921) used detailed analyses of surface observations to describe the vertical deformation and subsequent fracture of a warm frontal zone that resulted from the frontal

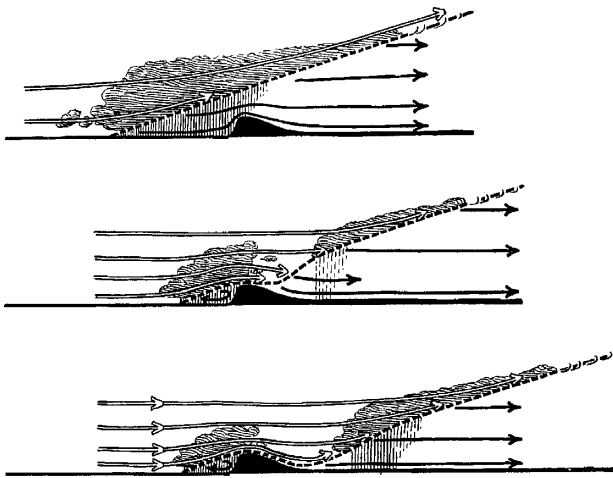


Fig. 2. Schematic depiction of topographic blocking and deformation of a warm front making landfall in Norway. From Bjerknes and Solberg (1921)

interaction with the complex topography of central Norway. Their analyses indicated that strong winds in the lee of the Norwegian highlands often occurred as the near-surface frontal zone passed over the steep topography (e.g., Fig. 20b of Bjerknes and Solberg, 1921). Bjerknes and Solberg hypothesized that both upstream blocking and adiabatic expansion upon lee-side descent contribute to frontal modification as depicted in their conceptualization of a land-falling warm front passing a mountain ridge (Fig. 2). These Norwegian events are similar to strong lee-side winds associated with Alpine foehn conditions, which are common in the pre cold-frontal environment characterized by strong cross-Alpine flow (e.g., Hoinka, 1985; Seibert, 1990).

Numerous observational studies (e.g., Müller and Sladkovic, 1990; Volkert et al., 1991) and numerical studies (e.g., Bannon, 1984, Williams et al., 1992) have shown that fronts tend to weaken on the windward sides of mountains and strengthen again on the lee slopes. Fronts have a tendency to steepen on the downslope side and become distorted in the presence of strong flow (Zong and Xu, 1997). Schuman (1987) noted that the impedance and deformation of a low-level frontal zone by orography will be greater when \hat{h} is large, a shallow and intense baroclinic zone exists, the front-normal velocity is small, and the mean-state stratification is large. The scaling parameters that control atmospheric flow response

to a front impinging on an obstacle include \hat{h} and the Rossby number ($R_o = U/fL$), where f is the Coriolis parameter, and L is the mountain half-width scale. As a result of this balanced response, the maximum extent of the decelerated region upstream of a mountain associated with blocking is on the order of the Rossby deformation radius ($L_R = Nh_m/f$) (Pierrehumbert and Wyman, 1985).

3. Model architecture

The atmospheric portion of the Navy's Coupled Ocean-Atmospheric Mesoscale Prediction System (COAMPS) (Hodur, 1997) was used to simulate the Oppdal windstorm. COAMPS is a finite-difference approximation to the fully compressible, nonhydrostatic equations that govern atmospheric motions. In this study, the equations are solved in three dimensions on four nested grid meshes with a terrain-following vertical coordinate, σ_z (Gal-Chen and Somerville, 1975). The finite difference schemes are of second order accuracy in time and space. A time splitting technique that features a semi-implicit treatment in the vertical for the acoustic modes enables efficient integration of the compressible equations (Klemp and Wilhelmson, 1978; Durran and Klemp, 1983).

The short- and long-wave radiative processes are parameterized following Harshvardhan et al. (1987). The planetary boundary layer and free-atmospheric turbulent mixing and diffusion are modeled using a prognostic equation for the turbulent kinetic energy (TKE) budget based on the level 2.5 formulation of Therry and LaCarrère (1983). Counter gradient correction terms to the vertical fluxes are included for the potential temperature and water vapor equations. The surface fluxes are computed following the Louis (1979) formulation, which makes use of the flux-profile relationships and Monin-Obukhov similarity theory. The surface energy budget is based on the force-restore method. The subgrid-scale moist convective processes are parameterized using an approach following Kain and Fritsch (1993). The grid-scale evolution of the moist processes are explicitly predicted from budget equations for cloud water, cloud ice, raindrops, snowflakes, and water vapor (Rutledge and Hobbs, 1983).

The computational domain for the present study was configured with four horizontally nested grids of 85×85 , 73×73 , 97×97 , and 145×145 points, respectively. The locations of the grid meshes are shown in Fig. 1. The horizontal grid increments of the computational meshes were 27 km, 9 km, 3 km, and 1 km, respectively. The model top was at 31 km with 38 irregularly spaced vertical levels and 14 levels in the lowest 1.5 km to sufficiently resolve the boundary-layer processes. Reflection of waves at the upper boundary was suppressed by a gravity wave absorbing layer using a Rayleigh damping technique in the upper 13 km of the model domain based on the work of Durran and Klemp (1983).

A 24-h COAMPS simulation, beginning at 0000 UTC 31 January 1995, utilized an incremental update data-assimilation procedure that enabled mesoscale circulations to be retained in the analysis increment fields. The initial fields for the nonhydrostatic model were created from multi-variate optimum interpolation analyses of upper-air sounding, surface, aircraft, and satellite data that were quality controlled and blended with the 12-h COAMPS forecast fields based on the incremental update methodology. Real-data lateral boundary conditions made use of Navy Operational Global Atmospheric and Prediction System (NOGAPS, Hogan et al., 1991) forecast fields following Davies (1976). It follows that use of COAMPS in this type of application closely emulated a real-time numerical prediction system in spite of the simulations being performed in a hindcast mode.

The topographic data were taken from the U.S. Defense Mapping Agency's 100-m resolution data set. The model terrain fields for the third ($\Delta x = 3$ km) and fourth mesh ($\Delta x = 1$ km), shown in Fig. 3, indicate that numerous steep canyons and valleys are embedded in the Norwegian highlands and further underscores the complex nature of the topography of this region. The Oppdal Valley and the village of Oppdal are located on the northern slope of the Norwegian massif and downstream from the highlands of the Dovre region. The model topographic data is representative of the complex local topography, with several mountain peaks to the south of the Oppdal Valley > 1800 m and a 1500 m mountain located immediately to the

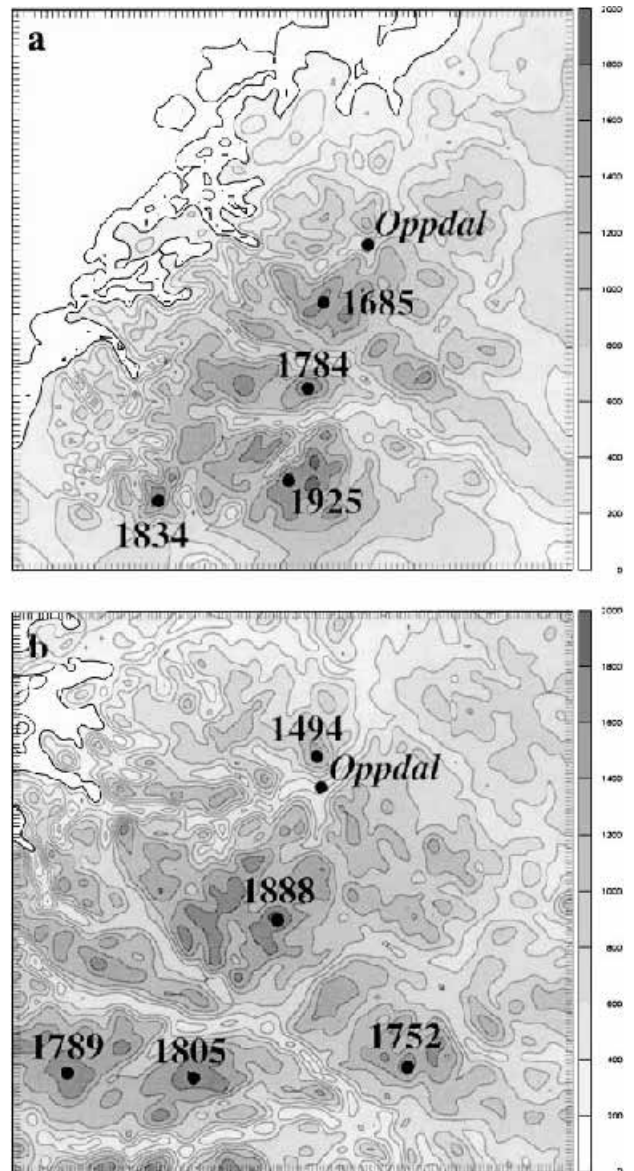


Fig. 3. Terrain field (shaded and contoured every 200 m) and noteworthy elevations for the (a) 3-km and (b) 1-km resolution grids

north of the valley and downstream of the low-level flow.

4. Synoptic-scale and frontal-scale perspective

The discussion of the synoptic-scale and frontal-scale evolution is based on the 24-h COAMPS simulation. The surface and 850-hPa fields for the 6-h, 12-h, and 18-h simulation times are shown in Figs. 4, 5, and 6, respectively. The results for 0600 UTC 31 January 1995 (Fig. 4a) show a mature cyclone with a minimum central

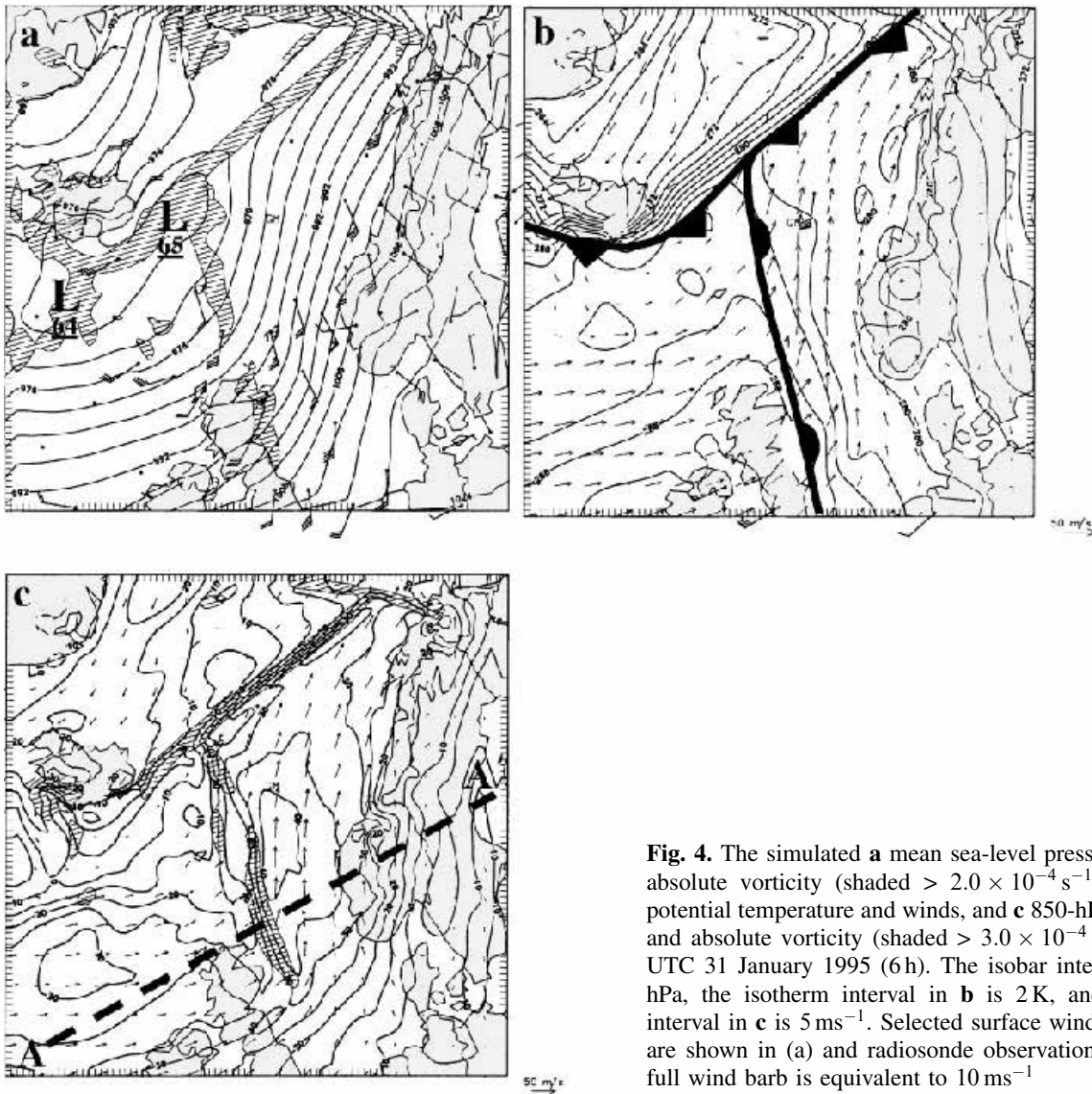


Fig. 4. The simulated **a** mean sea-level pressure and 10-m absolute vorticity (shaded $> 2.0 \times 10^{-4} \text{ s}^{-1}$), **b** 850-hPa potential temperature and winds, and **c** 850-hPa wind speed and absolute vorticity (shaded $> 3.0 \times 10^{-4} \text{ s}^{-1}$) for 0600 UTC 31 January 1995 (6 h). The isobar interval in **a** is 4 hPa, the isotherm interval in **b** is 2 K, and the isotach interval in **c** is 5 ms^{-1} . Selected surface wind observations are shown in (a) and radiosonde observations in (b). One full wind barb is equivalent to 10 ms^{-1} .

pressure of 964 hPa located in the Norwegian Sea between Norway and Iceland. A noteworthy feature of this situation is the well-defined warm front, which extends from the cyclone center southeastward to the east coast of Scotland. The 850-hPa potential temperature field at 0600 UTC (Fig. 4b) shows the moderate baroclinicity of the warm front situated between the westerly flow over the North Atlantic and southerly flow over the Norwegian Sea. A well-defined arctic front in low-level potential temperature and vorticity (Figs. 4a and 4c) extended from the northern coast of Norway to south of Iceland and is not a focus of this study. The 850-hPa wind field at 0600 UTC (Fig. 4c) shows the strong cyclonic shear within the warm front and associated

southerly jet with a maximum $> 40 \text{ ms}^{-1}$ in the cold air ahead of the front. Cyclonic vorticity maxima at the surface (Fig. 4a) and 850-hPa (Fig. 4c) are collocated with the baroclinicity of the warm front. Numerous near-surface observations from commercial petroleum drilling platforms in the North Sea show southerly winds $> 25 \text{ ms}^{-1}$ preceding the surface front (Fig. 4a) in close agreement with the simulated low-level winds.

By 1200 UTC 31 January (12 h), the warm front had progressed eastward toward the coast, where it was deformed by the steep topography of southern and central Norway with an enhancement of the pre-frontal jet (Fig. 5). The simulated sea-level pressure gradient and surface geo-

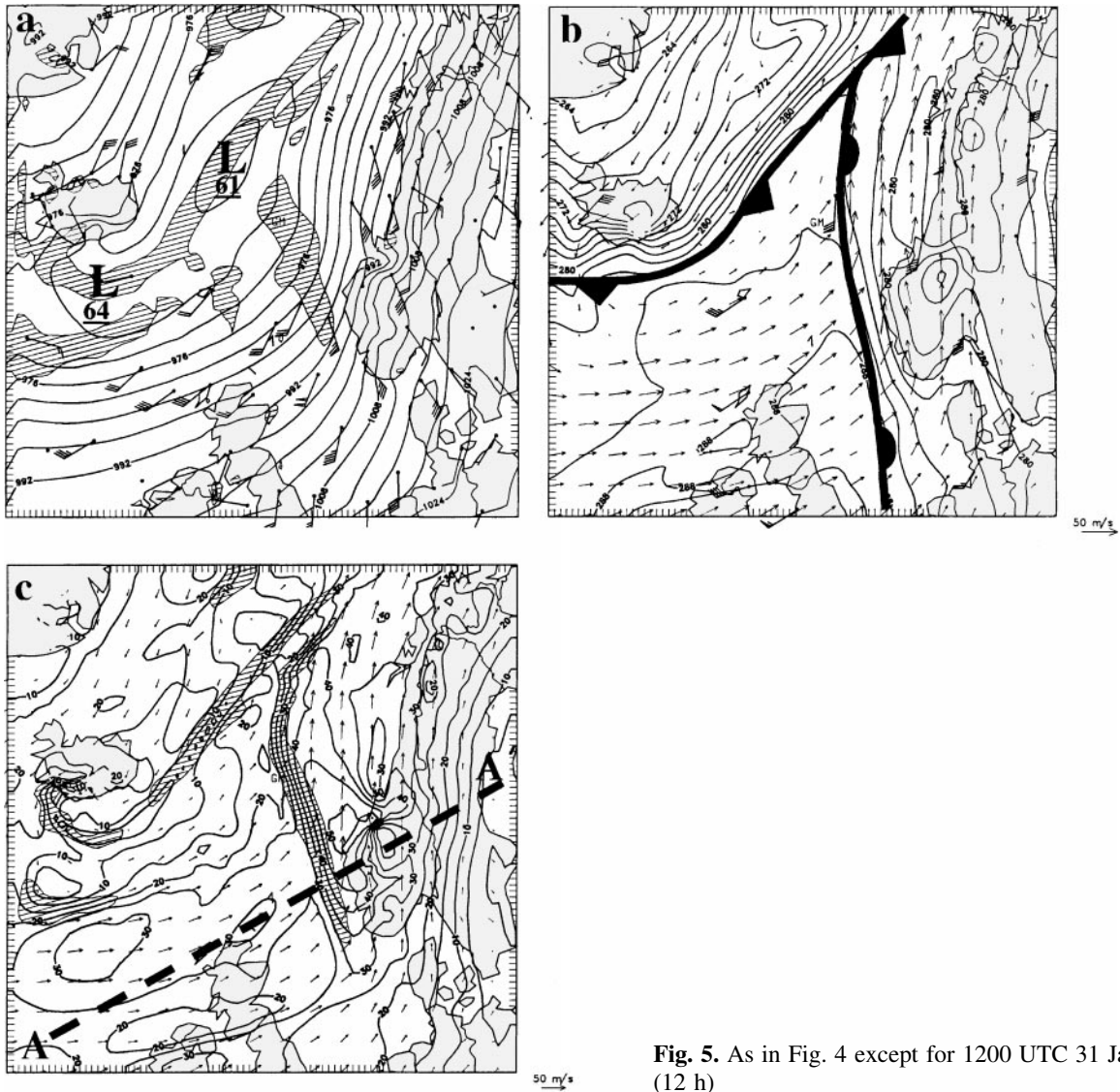


Fig. 5. As in Fig. 4 except for 1200 UTC 31 January 1995 (12 h)

strophic winds immediately upstream of the steep topography increased by $\sim 25\%$ during the previous 6-h (Fig. 5a). Surface observations over the North Sea document distinct cyclonic shear across the warm front, with southwesterly flow in the cold air. The frontal baroclinicity and ambient flow associated with the low-level jet intensified as the warm front approached the Norwegian coast (Fig. 5b). The realism of the simulated mesoscale structures is attested to by the close agreement between the model and the observed 850-hPa winds (Fig. 5b). As the southerly low-level jet ascended the steep Norwegian orography, a substantial mountain-wave disturbance formed in the vicinity of Oppdal, leeward of the mountainous region. An

850-hPa wind-speed maximum $> 50 \text{ ms}^{-1}$ developed along the lee slopes concurrent with an intensification of the low-level cyclonic shear and vorticity (Fig. 5c). In response to flow blocking and frontal contraction processes, the low-level jet attained a maximum speed of $\sim 56 \text{ ms}^{-1}$ at 0900 UTC 31 January (9 h). The warm/cold dipole in the 850-mb potential temperature field was a manifestation of the low-level mountain wave (Figs. 5b). The presence of mountain waves and corresponding strong descent in the lee of the Norwegian highlands is consistent with a well-defined cloud-free region in the 1223 UTC 31 January infrared satellite image (Fig. 7). A large area of clouds was present along the warm front and extended

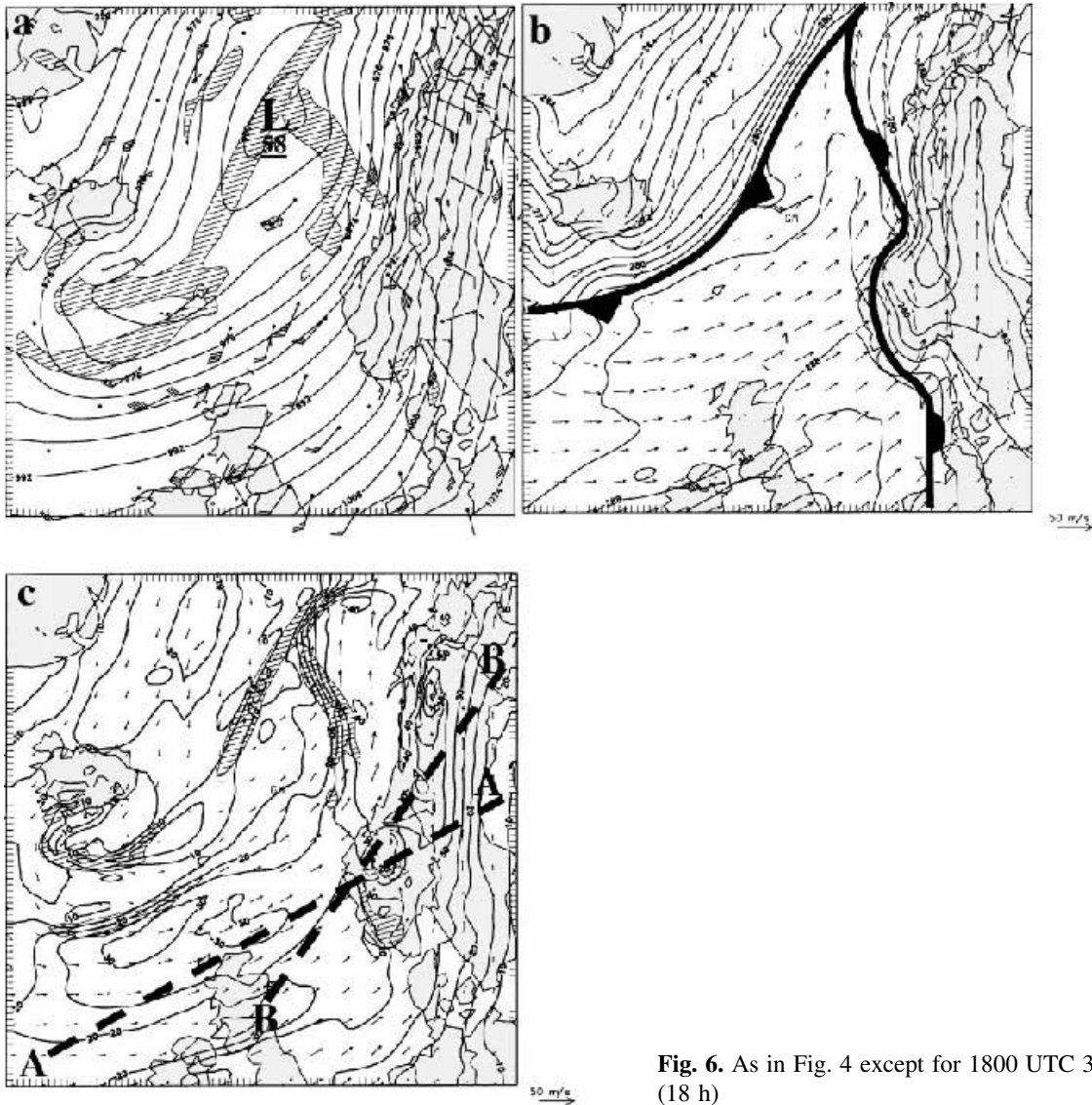


Fig. 6. As in Fig. 4 except for 1800 UTC 31 January 1995 (18 h)

eastward in a region of sloped ascent along the frontal zone, overriding the relatively cool air over Scandinavia.

The presence of topographically-generated gravity waves in the lee and blocking upstream of the central Norwegian mountains is particularly evident in the 18-h simulation of sea-level pressure and 10-m vorticity for 1800 UTC 31 January (Fig. 6a). The warm front was significantly distorted, and its eastward movement at low levels was impeded by the Norwegian topography to the west and south (Fig. 6b), similar to that described by Bjerknes and Solberg (1921) (e.g., Fig. 2). Adiabatic descent and warming contributed to the distortion of frontal properties in the lee. The observations show that strong

near-surface flow $> 25 \text{ ms}^{-1}$ (Fig. 6a) was present in the vicinity of the warm front. The portion of the warm front over the adjacent Norwegian Sea retained its integrity, including the strong 850-hPa thermal gradient (Fig. 6b), and attendant low-level jet, and vorticity filament (Fig. 6c).

The evolution of the vertical structure of the warm frontal zone and the modulation by topography is illustrated by a series of vertical sections oriented normal to the low-level baroclinic zone, along vertical projection line AA' (Figs. 4c, 5c, and 6c). At 0600 UTC 31 January (6 h), the cross section of potential temperature (Fig. 8a) indicates that prior to landfall, the low-level thermal gradient of the warm front was diffuse, with a weak static stability layer aloft

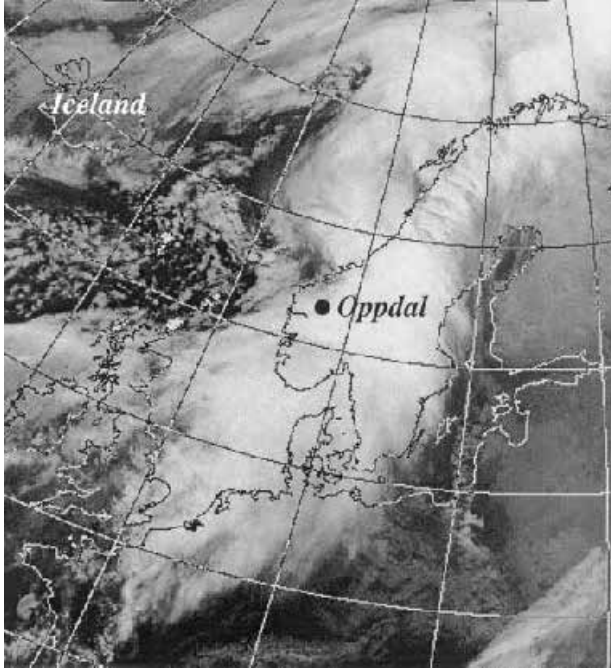


Fig. 7. Infrared satellite image for 1223 UTC 31 January 1995

arising from the vertical gradient of latent heating above the front. A well-defined low-level jet $\sim 36 \text{ ms}^{-1}$ was situated on the cold side of the baroclinic zone (Fig. 8b). By 1200 UTC (12 h), the topographic blocking led to a significant steepening of the front slope, as well as a doubling of the 800-hPa potential temperature gradient located just above the mountain top (Fig. 8c). The front-normal wind component of the low-level jet (Fig. 8d) increased from 36 ms^{-1} to $\sim 43 \text{ ms}^{-1}$ simultaneously with the frontal contraction. At 1800 UTC (18 h), topographic deformation of the warm front thermal gradient (Fig. 8e) and cross-front vorticity (Fig. 8f) was evident. A narrow front-normal wind-speed maximum was maintained along the upwind slope, while the main core of the low-level jet moved in the lee of the mountain peaks (Fig. 8f).

The role of the topography in deforming the warm front is further illustrated by a comparison of the simulations with and without topography, shown along the vertical projection line BB' (Fig. 6c) of Figs. 9a and b, respectively. The simulation with topography (Fig. 9a) has characteristics in common with the Bjerknes and Solberg (1921) schematic (Fig. 2):

- i) the impedance of the lower portion of the warm front upwind of the mountains,
- ii) the more rapid downstream movement of the upper-portion of the front, and
- iii) a mountain wave signature that separates the precipitation and clouds into two distinct regions.

One portion of the precipitation remained nearly stationary above the low-level warm front and upwind side of the coastal topography, whereas a second region was forced by frontal-scale ascent that propagated eastward with the upper portion of the warm front. The front retained a more continuous vertical structure in the absence of topography (Fig. 9b) similar to the warm front in the offshore stage (Fig. 8a).

In order to investigate the kinematics of frontal deformation by topography, consider the Lagrangian rate of change of the gradient of the virtual potential temperature (θ_v) through the kinematic frontogenesis equation for virtual potential temperature, defined as:

$$\begin{aligned} \frac{d}{dt} |\nabla \theta_v| = & |\nabla \theta_v|^{-1} \left\{ - \left[\left(\frac{\partial \theta_v}{\partial x} \right)^2 \frac{\partial u}{\partial x} + \left(\frac{\partial \theta_v}{\partial y} \right)^2 \frac{\partial v}{\partial y} \right] \right\} \\ & - |\nabla \theta_v|^{-1} \left[\left(\frac{\partial \theta_v}{\partial x} \frac{\partial \theta_v}{\partial y} \right) \left(\frac{\partial \omega}{\partial x} + \frac{\partial \omega}{\partial y} \right) \right] \\ & + |\nabla \theta_v|^{-1} \left[\frac{\partial \theta_v}{\partial x} \frac{\partial}{\partial x} \left(\frac{d\theta_v}{dt} \right) + \frac{\partial \theta_v}{\partial y} \frac{\partial}{\partial y} \left(\frac{d\theta_v}{dt} \right) \right] \end{aligned}$$

where ω is the vertical velocity, and u and v are the horizontal wind components. The first two terms on the right-hand side of (1) represent the contribution of the deformation field to the frontogenesis and include both horizontal confluence and horizontal shear effects. The twisting or tilting term is denoted by the third term. The fourth term on the right-hand side represents the frontogenesis due to horizontal gradients of diabatic heating.

The terms in the frontogenesis equation were evaluated for the full physics simulation and a simulation without topography. The results for 1500 UTC 31 January (15 h), shown in Fig. 10, reveal the complex mesoscale response to steep topography. The warm front is strengthened, especially in the lee, by topographic deformation associated with the high-amplitude mountain

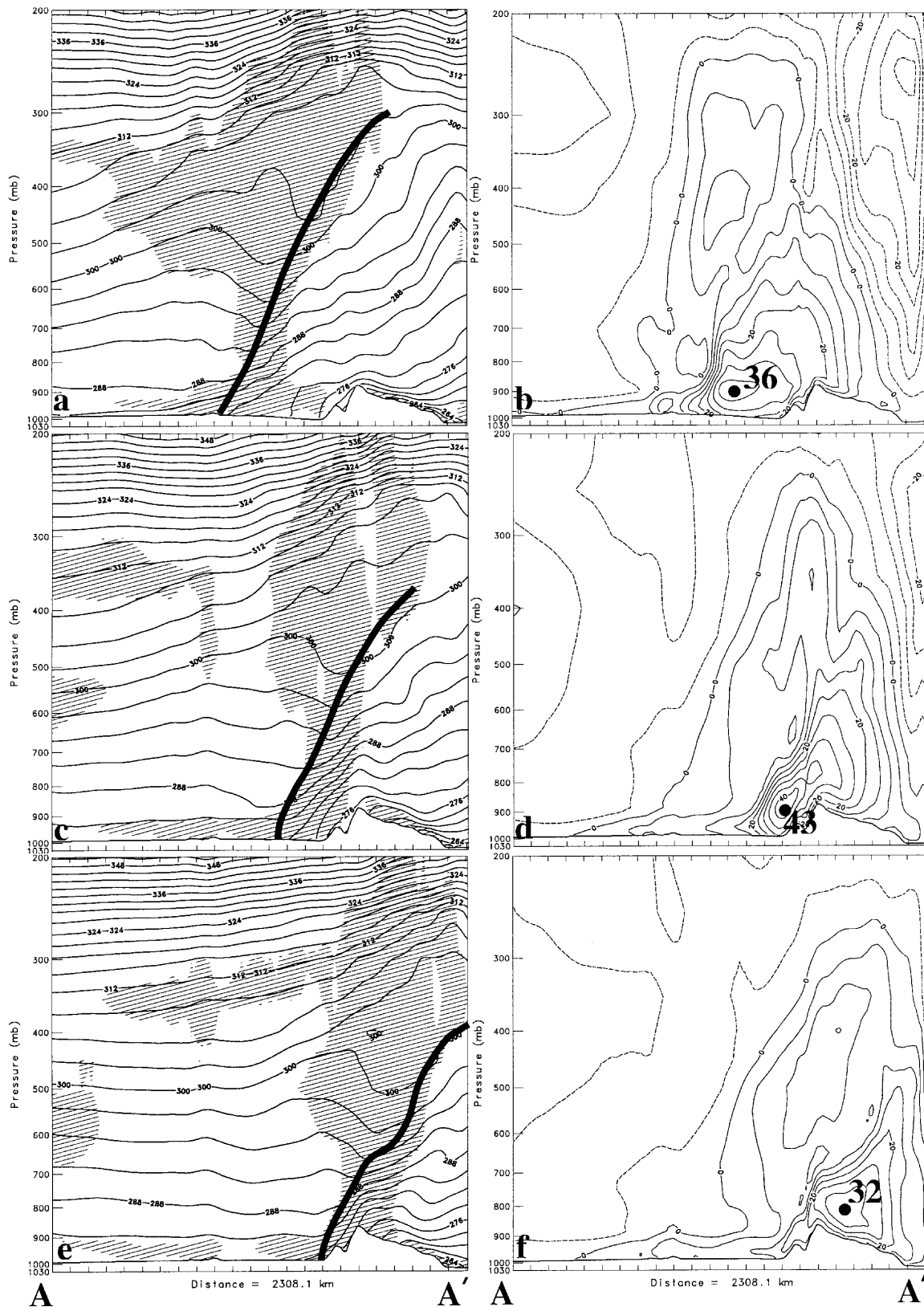


Fig. 8. Vertical section along line AA' (Figs. 4c, 5c, and 6c) of potential temperature (3 K) (a, c, e) and section-normal winds (5 m s^{-1}) (b, d, f) for 0600 UTC (a, b), 1200 UTC (c, d) and 1800 UTC (e, f) 31 January 1995. The relative humidity > 90% is shaded

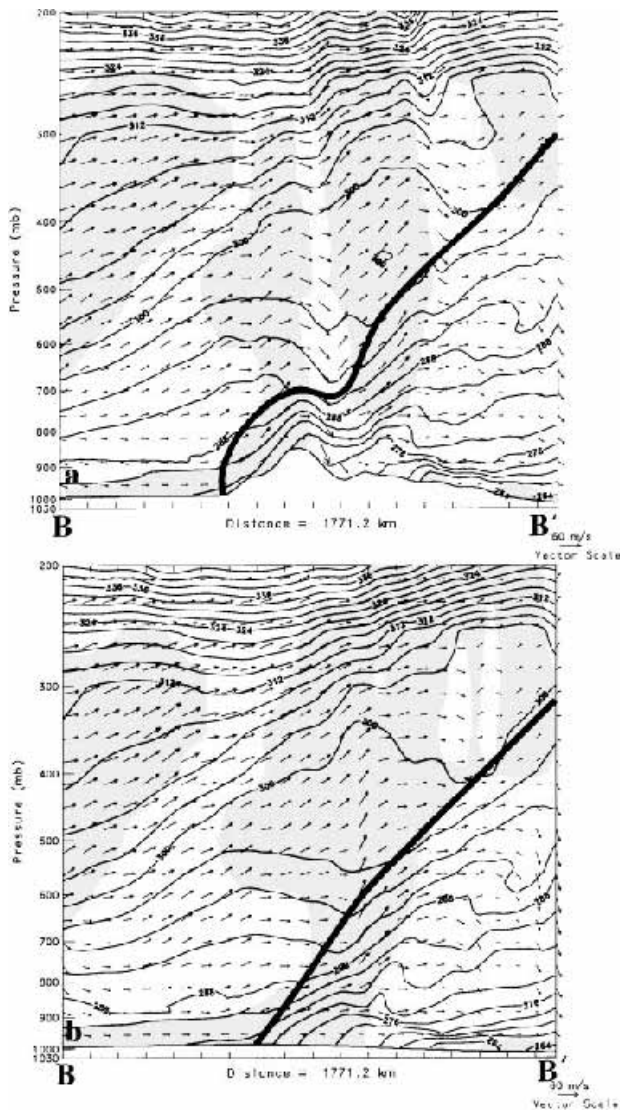


Fig. 9. Vertical cross section along line BB' (Fig. 6c) of potential temperature and along section winds for the **a** full-physics simulation and **b** simulation without topography for 1800 UTC (18 h) 31 January 1995. The relative humidity >90% is shaded. The isotherm interval is 3 K. The wind arrows are plotted every 10 grid points. The heavy solid line denotes the warm front inversion

wave (Fig. 10a). Contribution of the tilting term leads to an intense region of frontolysis immediately downstream of the strongest region of frontogenesis. This frontogenesis/frontolysis dipole, which is a result of the vertical motion and static stability anomalies associated with the large-amplitude mountain wave, acts to strengthen and deform the warm front in the horizontal as well as the vertical. Enhanced regions of frontogenesis are apparent upstream of the steepest topography as a result of low-level

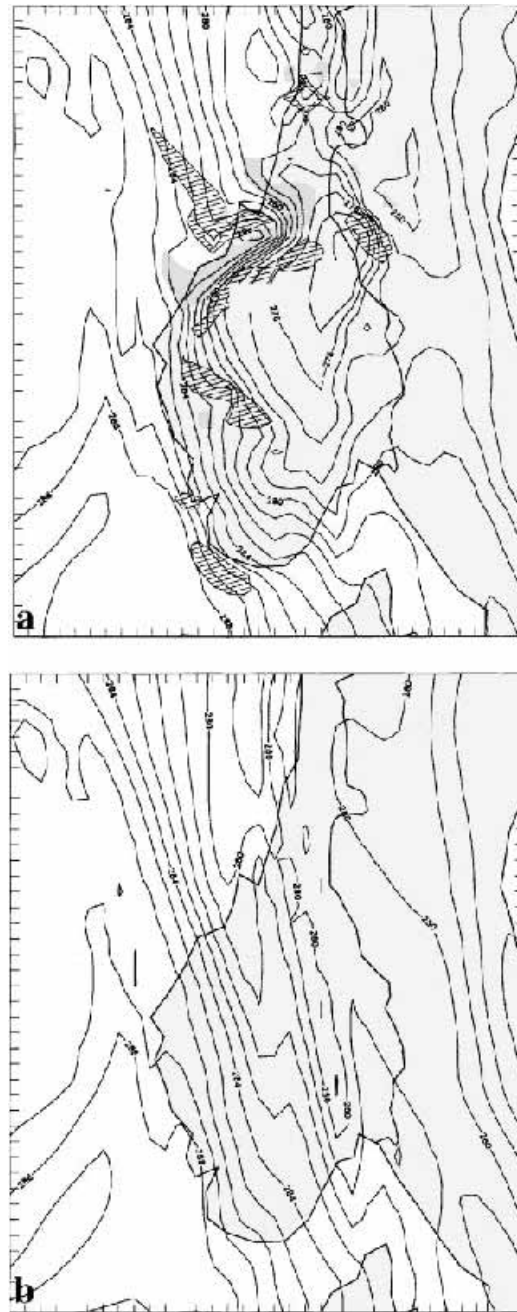


Fig. 10. The 850-hPa potential temperature for the **a** full-physics and **b** no-terrain simulations for a portion of the coarse mesh domain for 1500 UTC (15 h) 31 January 1995. The isotherm interval is 1 K. Frontogenesis $>5 \text{ K} (10 \text{ km } 6 \text{ h})^{-1}$ is denoted by the hatched region, and $< -5 \text{ K} (10 \text{ km } 6 \text{ h})^{-1}$ is represented by the dark shaded region

blocking effects. The simulation without topography has a quasi-linear frontal structure at 850 hPa with locally weaker frontogenesis in central Norway (Fig. 10b). The maximum 850-hPa thermal gradient is strengthened by a factor of

three through the topographic deformation processes in the lee of the highest topography. In summary, the strengthening of the mesoscale thermal gradients is clearly tied to frontogenesis through differential vertical motion or tilting.

5. Fine-scale windstorm aspects

At 1200 UTC 31 January (12 h), the 300-m AGL wind field for the 3-km resolution grid (Fig. 11a)

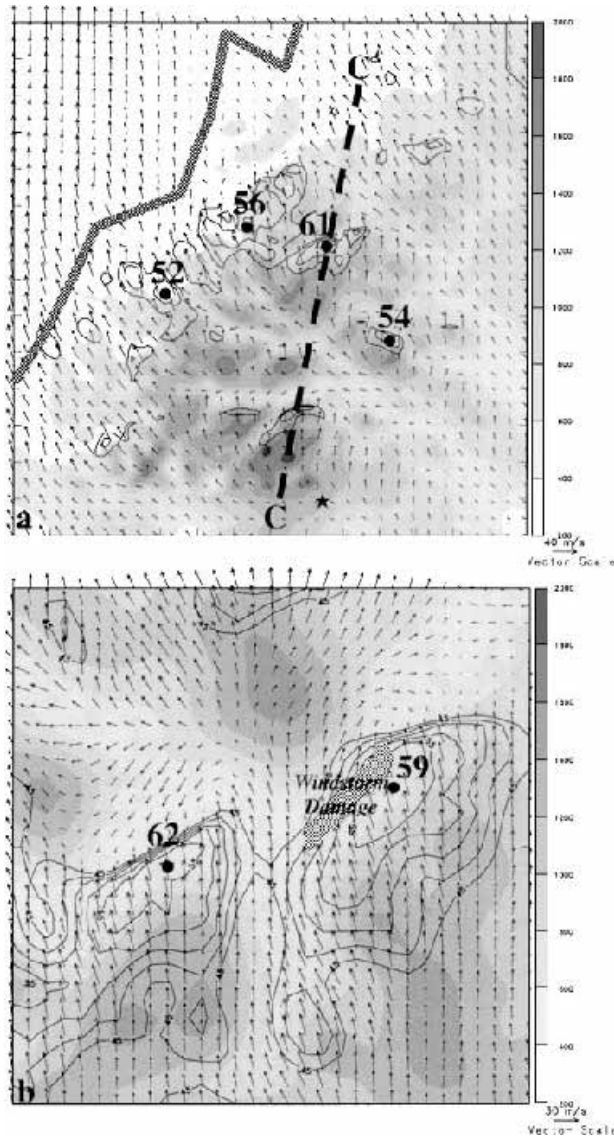


Fig. 11. The simulated 300-m AGL wind field for the **a** 3-km resolution and **b** a subdomain of 1-km resolution grids. The isotachs are shown $>45 \text{ ms}^{-1}$ at an interval of 5 ms^{-1} in (a) and 2.5 ms^{-1} in (b). The terrain field for the 3-km and 1-km resolution meshes are represented by the shading in (a) and (b), respectively. Wind arrows are plotted every third point in (a) and every point in (b)

indicates a maximum speed of $>60 \text{ ms}^{-1}$ located within the Oppdal Valley. Several other areas contain wind speeds $>50 \text{ ms}^{-1}$, in particular to the north and west of the Oppdal Valley. All regions of high wind speed are located in the lee of the highest topography within the Norwegian massif. Orographic blocking and deflection are apparent upstream of the mountain peaks, resulting in easterly valley flows. The 300-m AGL wind field valid at 1400 UTC (14 h) for a sub-domain of the 1-km grid (Fig. 11b) indicates that, despite the known difficulties in predicting low-level winds in complex terrain, the model simulated maximum wind speed is coincident within the region of observed windstorm damage in the Oppdal Valley. Observational estimates from the damage survey suggest that the windstorm occurred at approximately 1500 UTC with wind gusts $>60 \text{ ms}^{-1}$ (Harstveit et al., 1995).

Figure 12 presents a sequence of south-north oriented vertical cross sections of potential temperature and horizontal wind speed, constructed parallel to the low-level flow and along vertical projection line CC' of Fig. 11a. The 0600 UTC (6-h) potential temperature cross section (Fig. 12a) reveals a two-layer structure within the troposphere, with high stability in the low-levels below 600 hPa associated with the warm frontal inversion, and weaker stability aloft in the 300–400 hPa layer. The 0600 UTC (6-h) wind-speed cross section (Fig. 12b) indicates that a layer of significant low-level wind speeds $>25 \text{ ms}^{-1}$ was present below $\sim 700 \text{ hPa}$, with weaker cross-mountain wind speeds less than 10 ms^{-1} above 500 hPa. The maximum cross-mountain wind speeds are present near the mountain peak (Fig. 12b).

The 1200 UTC (12-h) potential temperature cross section (Fig. 12c) valid near the time of the observed windstorm indicates that the stratification below $\sim 600 \text{ hPa}$ increases concurrent with destabilization in the 350–500 hPa layer. The warm frontal inversion above the mountain top, often associated with downslope windstorm events (e.g., Colson, 1954; Brinkman, 1974; Durran, 1990), has undergone substantial vertical distortion. Wave amplification within the Oppdal Valley is noted below 500 hPa with the maximum amplitude $>2.5 \text{ km}$ height deviation of the 297 K isentropic surface. In this case, the wave is

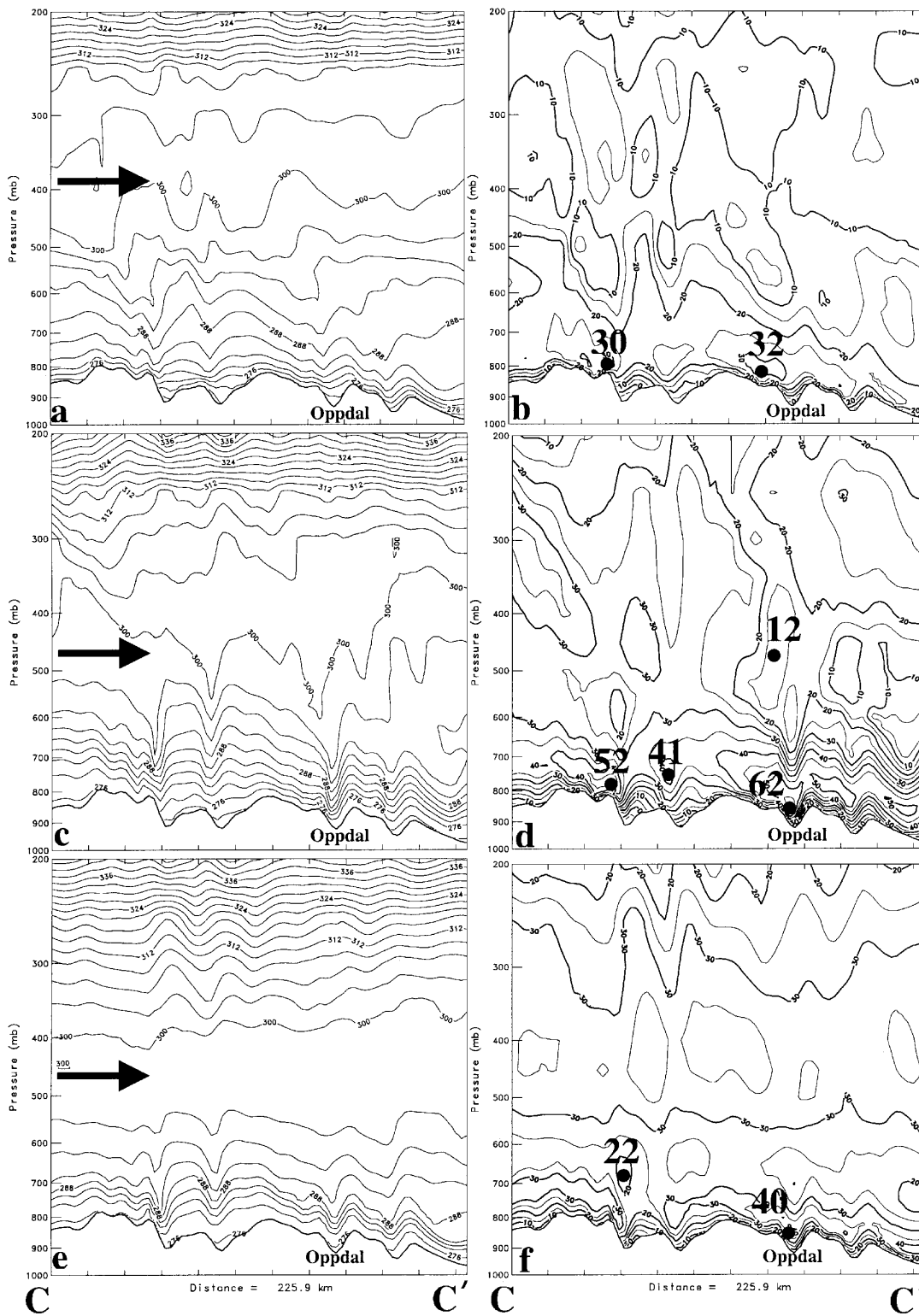


Fig. 12. Vertical section along line CC' (Fig. 11a) of the potential temperature (3 K) (a, c, e) and along-section wind speed (5 ms^{-1}) for 0600 UTC (a, b), 1200 UTC (c, d) and 1800 UTC (e, f) 31 January 1995

confined to the lower troposphere, unlike the full troposphere, large-amplitude waves found in other cases (e.g., Lilly, 1978). The lack of substantial vertical wave tilt throughout the wave life cycle (e.g., Figs. 12a and 12c) suggests that the vertical propagation of the gravity wave energy may be trapped. The largest cross-mountain wind speeds at 1200 UTC (12 h) (Fig. 12d) are $> 55 \text{ ms}^{-1}$ at 300 m above the valley. Large vertical shear is apparent in the cross section, with the mean cross-mountain wind speed $\sim 35 \text{ ms}^{-1}$ below 700 hPa and $< 20 \text{ ms}^{-1}$ above 600 hPa.

By 1800 UTC (18 h), the low-level stratification remains large, and the 400–550 hPa static stability continues to weaken (Fig. 12e). However, the cross-mountain wind speed (Fig. 12f) indicates that despite the depth of the strong low-level flow ($> 30 \text{ ms}^{-1}$) increasing slightly, the windstorm in the lee diminishes to $< 45 \text{ ms}^{-1}$ over the previous 6 h as the low-level warm front deforms (Fig. 9a).

Figure 13 shows the time-height evolution of the cross-mountain wind speed and potential temperature at a grid point (3-km resolution grid)

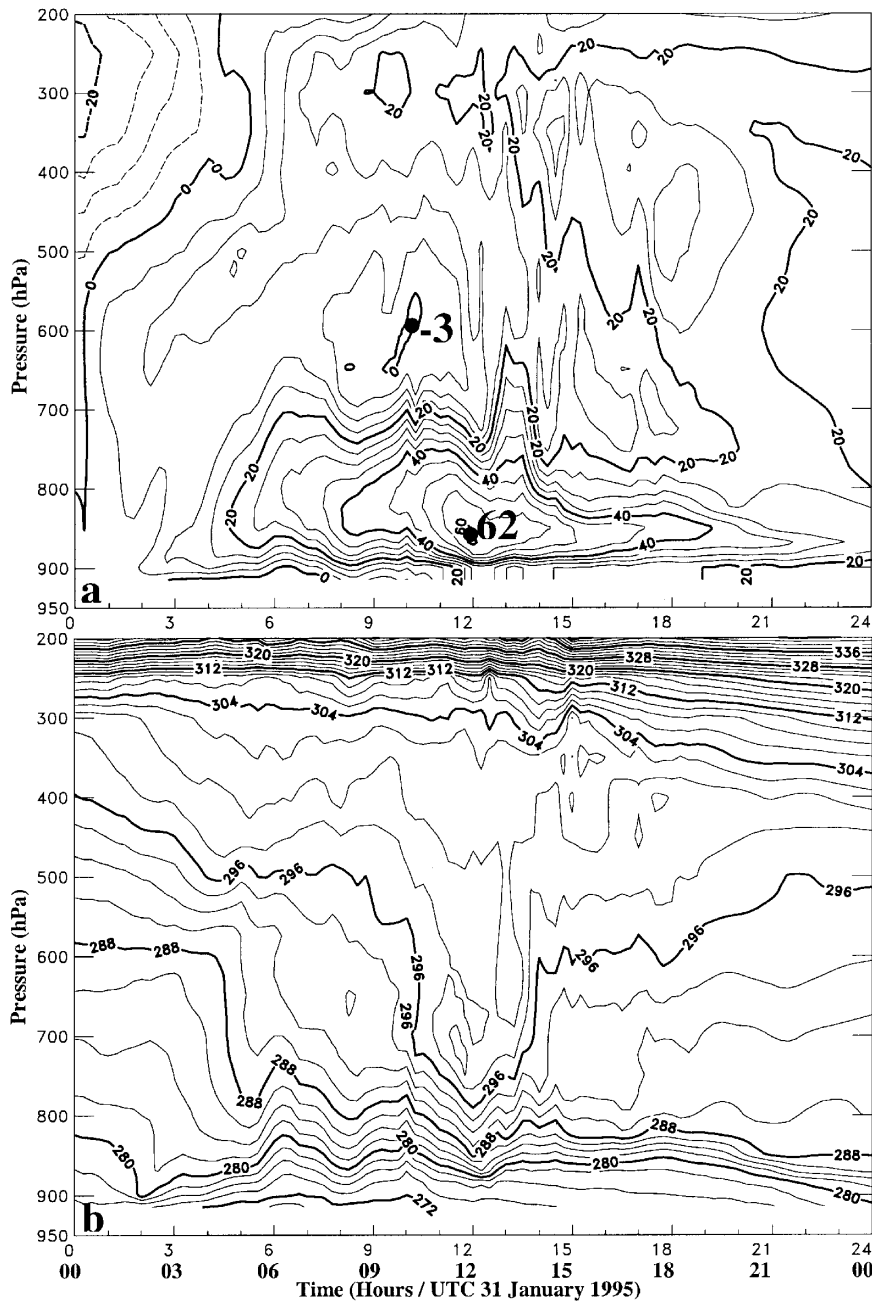


Fig. 13. Time-pressure section of the **a** cross-mountain wind speed and **b** potential temperature from 0000 UTC 31 January through 0000 UTC 01 February 1995 (0–24 h) for a grid point near Oppdal on the 3-km resolution grid. The isotach interval is 5 ms^{-1} in (a), and the isotherm interval is 5 K in (b)

within the region of the windstorm damage. The rapid increase of the cross-mountain wind speed maximum and its descent to near the surface are apparent between 0300 UTC (3 h) and 1200 UTC (12 h) (Fig. 13a). Between 0900 UTC (9 h) and 1200 UTC (12 h), the 550–650 hPa cross-mountain flow decreases by $> 10 \text{ ms}^{-1}$ and reverses, such that large vertical shear ($40 \text{ ms}^{-1}/100 \text{ hPa}$) develops in the 700–800 hPa layer. An increase in the low-level stratification below 750 hPa and a decrease between 500–700 hPa preceded the largest cross-mountain wind speeds (Fig. 13b). Overturning of the 600–750 hPa isentropic layer, a likely signature of low-level gravity wave amplification and breakdown, is apparent above the vertical shear layer during the time period when the cross-mountain wind speeds are $> 50 \text{ ms}^{-1}$.

The 1200 UTC (12 h) mean structure of the troposphere is represented (Fig. 14a) by vertical profiles of potential temperature and the cross-mountain wind component, averaged over a 25-grid point region upstream of the windstorm (location shown by the star in Fig. 11a). The profiles contain a two-layer structure characterized by i) large static stability below 700 hPa, ii) weak stability in the 350–500 hPa layer, and iii) strong southerly flow in excess of 30 ms^{-1} below 650 hPa.

Further general insight into the dynamics of this windstorm may be gained by considering the linear response to the mean state structure. Scorer (1949) made use of linear theory to show that wave energy may be trapped due to vertical variations in the mean state velocity and stability. For two-dimensional, inviscid, Boussinesq flow with no rotation ($f = 0$), the linearized, steady-state equations can be reduced to form a second-order partial differential equation for the perturbation vertical velocity (e.g., Scorer 1949; Alaka 1960)

$$\frac{\partial^2 w}{\partial x^2} + \frac{\partial^2 w}{\partial z^2} + l^2 w = 0, \quad (2)$$

where l is the Scorer parameter, defined as

$$l^2 = \frac{N^2}{U^2} - \frac{1}{U} \frac{\partial^2 U}{\partial z^2}. \quad (3)$$

Following Scorer (1949) and Durran and Klemp (1982), the necessary condition for the existence of mountain wave energy trapping for a two-layer

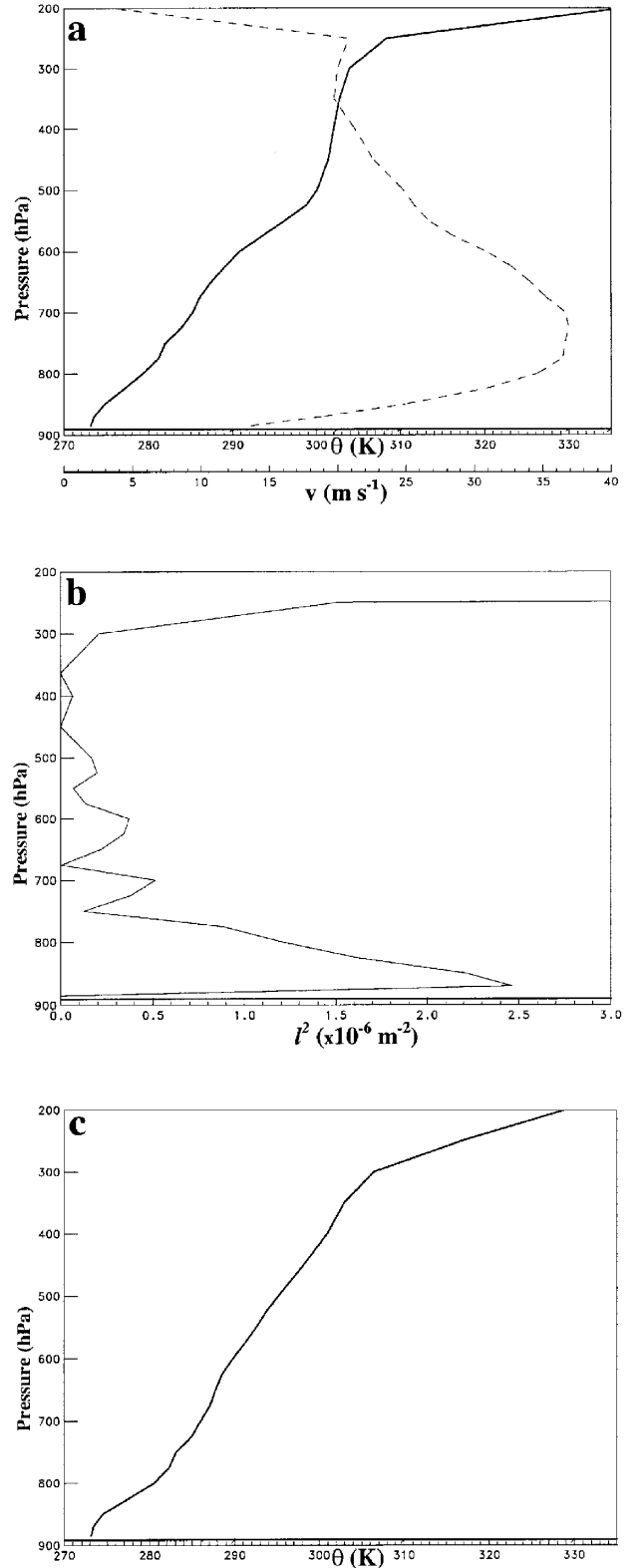


Fig. 14. Vertical profiles of **a** potential temperature (solid, K) and the v-wind component (dashed, ms^{-1}); **b** l^2 ($\times 10^{-6} \text{ m}^{-2}$), and **c** potential temperature (K) for the simulation without latent heating. The profiles are averaged over 25 grid points centered at the ‘ \star ’ in Fig. 11a

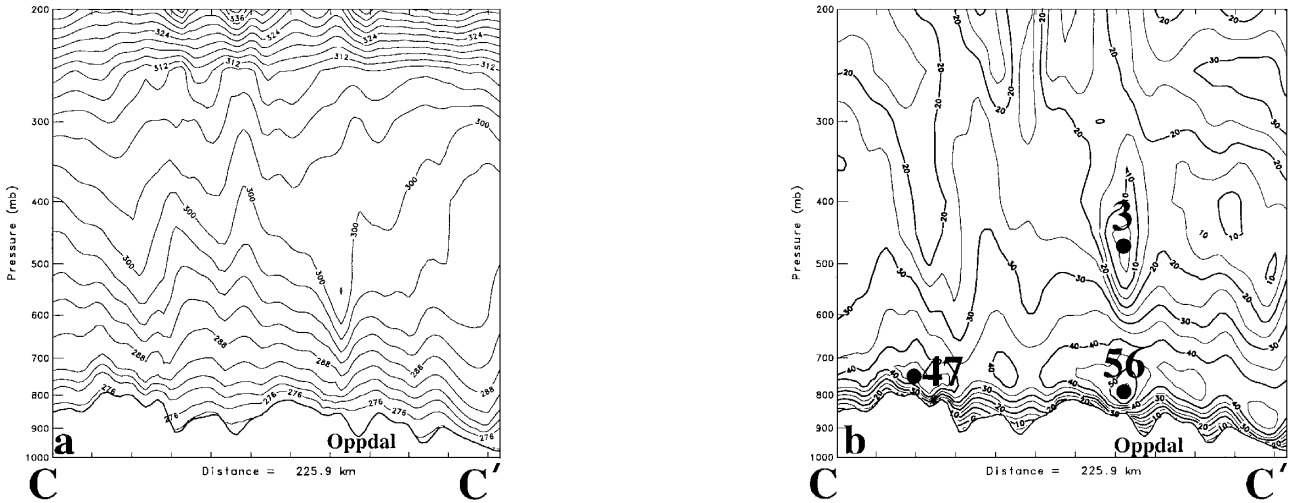


Fig. 15. Vertical section along line CC' (Fig. 11a) of **a** potential temperature (3 K) and **b** along-section wind speed (5 ms^{-1}) for 1200 UTC 31 January 1995 (12 h) for the simulation without latent heat processes

fluid that contains a discontinuity in l occurs when

$$l_L^2 - l_U^2 > \frac{\pi^2}{4H^2}. \quad (4)$$

For the present situation, a mean profile of l^2 is computed upstream of the Oppdal Valley valid at 1200 UTC (12 h) (Fig. 14b). Here, the Scorer parameter is characterized by a near two-layer structure with a rapid decrease with height above the lower troposphere. The criterion for trapped wave energy is satisfied in this highly idealized setting assuming $H \sim 1200 \text{ m}$, $l_L^2 \sim 2.2 \times 10^{-6} \text{ m}^{-2}$, and $l_U^2 \sim 0.2 \times 10^{-6} \text{ m}^{-2}$. However, the applicability of this highly idealized theory to a complex, three-dimensional flow is clearly limited. It is noteworthy that the two-layer mean state structure and ensuing windstorm dynamics are in marked agreement with the idealized numerical simulations of downslope windstorms presented in Durran (1986).

The origin of the strong low-level winds and enhanced static stability in the Oppdal Valley is clearly tied to the presence of the warm front. The sloping frontal inversion and vertical shear associated with the low-level jet contribute to the two-layer characteristics of the Scorer profile. Additionally, the weak stability aloft acts to reduce l in the upper layer. The origin of this layer of weak stability arises through the destabilizing effect of the vertical gradient in

latent heat associated with the maximum ascent above the warm front, as previously discussed (Figs. 8 and 9).

In order to gain further insight into the destabilizing effect of differential latent heating, a simulation was performed excluding the latent heating of condensation. The 1200 UTC (12-h) mean vertical profile of potential temperature (Fig. 14c) from this simulation upstream of the windstorm reveals a significantly larger 350–500 hPa static stability relative to the full-physics simulation (Fig. 14a). Trajectory analysis (not shown) provides further confirmation of the destabilization in the upper-levels resulting from the differential diabatic processes. In the full-physics simulation, latent heating contributed to a 6 K warming just above the warm front concurrent with adiabatic flow near the tropopause. This is also evident in the comparison of the cross sections of potential temperature and cross-mountain wind speed for the no-latent heating (Figs. 15a-b) and full-physics (Figs. 12c-d) simulations, valid near the time of the observed windstorm (1200 UTC). Note that in the absence of latent heating (Fig. 15), the wave amplitudes and cross mountain wind speeds, particularly within the Oppdal Valley, are significantly reduced in contrast to the full-physics simulation (Figs. 12c-d). Calculations of the Richardson number, R_i , ($N^2/(dU/dz)^2$) indicate that the full-physics simulation is characterized by a smaller

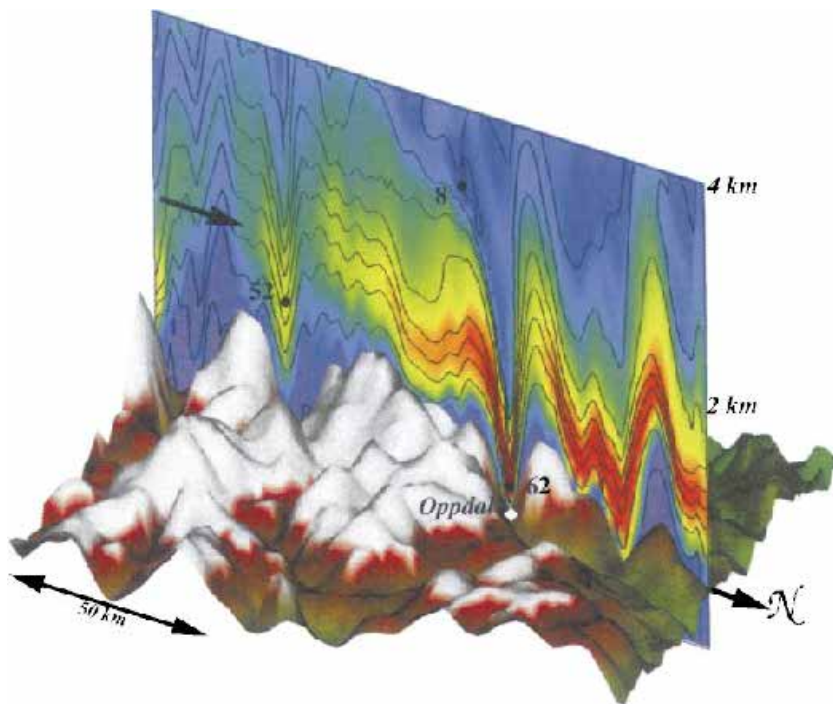


Fig. 16. Three-dimensional depiction of the 1-km resolution mesh results for a south-north vertical section of potential temperature (2 K) and wind speed (color shading) as viewed from the northeast for 1345 UTC 31 January 1995 (13.75 h). Red shading corresponding to wind speeds $> 55 \text{ ms}^{-1}$ and blue shading $< 15 \text{ ms}^{-1}$

midtropospheric R_i minimum than the simulation without latent heating. The mitigation of the downslope windstorm in this simulation without latent heating is apparently related to a resonant response to the modified mean-state stability and cross-mountain wind profiles. For example, Durran and Klemp (1982) found that in the presence of mid-level moisture, such as in the present study, lee waves may amplify when the height of the trapping interface is reduced due to resonant effects.

Figure 16 shows a south-north oriented vertical section of the wind speed and potential temperature, valid at 1345 UTC (13.75 h), for the 1-km resolution grid. The largest amplitude wave is situated above the Oppdal Valley, with characteristics consistent with the internal hydraulic amplification processes illustrated in the idealized simulations of Durran (1986). For the present study, qualitative analysis of the model results indicates the presence of supercritical flow in the lee concurrent with downward displacement of the low-level frontal inversion in the Oppdal Valley. Considering the three-dimensionality of the topography over Norway evident in Fig. 16 and the

complexity of the flow, the model predictive skill of the windstorm event is remarkable.

6. Concluding remarks

A mesoscale numerical simulation of an extreme downslope windstorm over the mountains of central Norway was undertaken to test the ability of a sophisticated numerical weather prediction system (COAMPS) to forecast extremely localized topographic flow over highly complex terrain. The simulation was used to identify key synoptic-scale and mesoscale characteristics of the event and to establish links with observational and theoretical studies of similar topographic flows. Since there were no direct observations to evaluate the representativeness of the simulation, indirect confirmation of the extreme wind event was inferred from widespread destruction of substantial buildings throughout the Oppdal valley. Clearly, the present study is not definitive in that few, if any, observations confirm the three-dimensional evolution of the mountain-wave amplification event. However, the study does reaffirm the

ability of high-resolution models to simulate frontal-scale contraction and associated diabatic processes, and the consequence of their interaction with complex orography.

The key findings and new insights arising from this study are

- i) mountain wave resonance and amplification arising from the interaction of a surface-based warm front and attendant lower tropospheric jet with complex orography,
- ii) sensitivity of the wave response to differential diabatic heating (vertical) gradients in the layer bounded by the tropopause and warm frontal ascent,
- iii) in contrast to previously studied idealized and observed windstorms characterized by strong flow response in the lower-stratosphere (e.g., Lilly, 1978; Clark and Peltier, 1977; Peltier and Clark, 1983), the wave response for the present study is trapped within the layer of large frontal stratification in the lower troposphere, and
- iv) wave amplification is consistent with the theoretically established two-layer hydraulic analogue (e.g., Durran, 1986).

It is imperative that future high-resolution simulations be evaluated with comparably resolved in situ and remote-sensing observing systems, such as will be deployed in support of gravity wave studies in the Mesoscale Alpine Programme (MAP) (Houze et al., 1998). Finally, the results of the study highlight the promising future for the utilization of high-resolution numerical simulations in advancing our understanding and predictability of three-dimensional complex topographic flows.

Acknowledgements

The research support for the first author was provided by the Naval Research Laboratory's (NRL) Orographic and Fetch-Limited Flows Research Option sponsored by the Office of Naval Research (ONR) grant N0001499F0068. The second author expresses appreciation to NRL-Monterey for sponsoring his collaborative visits to NRL through the support of ONR program element 0602435N. Computing time was supported in part by a grant of HPC time from the Department of Defense Shared Resource Center, Stennis Space Center, MS, and performed on a Cray T-90. Beneficial discussions with Dale Durran and Richard Reed are greatly appreciated. We thank Sigbjørn Grønås and Knut Helge Midtbø for valuable discussions

concerning observational aspects of the Oppdal downslope windstorms.

References

- Alaka MA (1960) The airflow over mountains. WMO Technical Note 34: 135 pp
- Bannon PR (1984) A semi-geostrophic model of frontogenesis over topography. *Beitr Phys Atmos* 57: 393–408
- Bjerknes J, Solberg H (1921) Life cycle of cyclones and the polar front theory of atmospheric circulation. *Geofys Publik* 3(1): 3–18
- Brinkman WAR (1974) Strong downslope winds at Boulder. *Mon Wea Rev* 102: 592–602
- Campins J, Jansa A, Benech B, Koffi E, Bessemoulin P (1995) PYREX observation and model diagnosis of the Tramontane wind. *Meteorol Atmos Phys* 56: 209–228
- Clark TL, Farley RD (1984) Severe downslope windstorm calculations in two and three spatial dimensions using anelastic interactive grid nesting: A possible mechanism for gustiness. *J Atmos Sci* 41: 329–350
- Clark TL, Peltier WR (1977) On the evolution and stability of finite amplitude mountain waves. *J Atmos Sci* 34: 1715–1730
- Colle BA, Mass CF (1998a) Windstorms along the western side of the Washington Cascade Mountains. Part I: A high-resolution observational and modeling study of the 12 February 1995 event. *Mon Wea Rev* 126: 28–52
- Colle BA, Mass CF (1998b) Windstorms along the western side of the Washington Cascade Mountains. Part II: Characteristics of past events and three-dimensional idealized simulations. *Mon Wea Rev* 126: 53–71
- Colson D (1954) Meteorological problems in forecasting mountain waves. *Bull Amer Meteor Soc* 35: 363–371
- Davies HC (1976) A lateral boundary formulation for multi-level prediction models. *Quart J Roy Meteor Soc* 102: 405–418
- Durran DR (1986) Another look at downslope windstorms. Part I: The development of analogs to supercritical flow in an infinitely deep, continuously stratified fluid. *J Atmos Sci* 43: 2527–2543
- Durran DR (1990) Mountain waves and downslope winds. *Atmospheric Process over Complex Terrain*. AMS Monograph 23: 59–81
- Durran DR (1992) Two-layer solutions to Long's equation for vertically propagating mountain waves: How good is linear theory? *Quart J Roy Meteor Soc* 118: 415–433
- Durran DR, Klemp JB (1982) The effects of moisture on trapped mountain lee waves. *J Atmos Sci* 39: 2490–2506
- Durran DR, Klemp JB (1983) A compressible model for the simulation of moist mountain waves. *Mon Wea Rev* 111: 2341–2361
- Eliassen A, Palm E (1960) On the transfer of energy in stationary mountain waves. *Geofys Publ* 22: 1–23
- Gal-Chen T, Somerville RCJ (1975) On the use of a coordinate transformation for the solution of the Navier-Stokes equations. *J Comput Phys* 17: 209–228
- Harshvardhan, Davies R, Randall D, Corsetti T (1987) A fast radiation parameterization for atmospheric circulation models. *J Geophys Res* 92: 1009–1015

- Harstveit K, Andresen L, Midtbø KH (1995) Downslope windstorms at Oppdal, Norway: Local description and numerical simulations. DNMI Report no. 23/95 Klima, 29 pp
- Hodur RM (1997) The Naval Research Laboratory's Coupled Ocean/Atmosphere Mesoscale Prediction System (COAMPS). *Mon Wea Rev* 125: 1414–1430
- Hogan TF, Rosmond TE (1991) The description of the U.S. Navy Operational Global Atmospheric Prediction System's spectral forecast model. *Mon Wea Rev* 119: 1786–1815
- Hoinka KP (1985) Observation of the air-flow over the Alps during a Foehn event. *Quart J Roy Meteor Soc* 111: 199–224
- Houze R, Kuettner J, Smith R (eds) (1998) Mesoscale Alpine Programme (MAP) U.S. Overview Document and Experiment Design. 69 pp. [Available from: U.S. MAP Programme Office, UCAR, JOSS, P.O. Box 3000, Boulder, CO 80307–3000]
- Kain JS, Fritsch JM (1993) Convective parameterization for mesoscale models: The Kain-Fritsch scheme. The Representation of Cumulus convection in Numerical Models, Meteor Monogr 46, Amer Meteor Soc 165–170
- Klemp JB, Durran DR (1987) Numerical modelling of bora winds. *Meteor Atmos Phys* 36: 215–227
- Klemp JB, Lilly DK (1975) The dynamics of wave induced downslope winds. *J Atmos Sci* 32: 320–339
- Klemp J, Wilhelmson R (1978) The simulation of three-dimensional convective storm dynamics. *J Atmos Sci* 35: 1070–1096
- Lilly DK (1978) A severe downslope windstorm and aircraft turbulence event induced by a mountain wave. *J Atmos Sci* 35: 59–77
- Lilly DK, Zipser EJ (1972) The Front Range windstorm of January 11, 1972, *Weatherwise* 25: 56–63
- Long RR (1953) Some aspects of the flow of stratified fluids. Part I: A theoretical investigation. *Tellus* 5: 42–58
- Louis JF (1979) A parametric model of vertical eddy fluxes in the atmosphere. *Bound-Layer Meteor* 17: 187–202
- Miles JW, Huppert HE (1969) Lee waves in a stratified flow. Part 4: Perturbation approximations. *J Fluid Mech* 35: 497–525
- Müller H, Sladkovic R (1990) Case studies of frontal passages in a mountain valley with direct access to the Bavarian pre-Alpine region results from the German Front Experiment 1987. *Meteor Atmos Phys* 43: 77–87
- Neiman PJ, Hardesty RM, Shapiro MA, Cupp RE (1988) Doppler lidar observations of a downslope windstorm. *Mon Wea Rev* 116: 2265–2275
- Peltier WR, Clark TL (1979) The evolution and stability of finite-amplitude mountain waves. Part II: Surface wave drag and severe downslope windstorms. *J Atmos Sci* 36: 1498–1529
- Peltier WR, Clark TL (1983) Nonlinear mountain waves in two and three spatial dimensions. *Quart J Roy Meteor Soc* 109: 527–548
- Pierrehumbert RT, Wyman B (1985) Upstream effects of mesoscale mountains. *J Atmos Sci* 42: 977–1003
- Rutledge SA, Hobbs PV (1983) The mesoscale and microscale structure of organization of clouds and precipitation in midlatitude cyclones. VIII: A model for the “seeder-feeder” process in warm-frontal rainbands. *J Atmos Sci* 40: 1185–1206
- Sarker RP, Calheiros RV (1974) Theoretical analysis of lee waves over the Andes as seen by satellite pictures. *Pure Appl Geophys* 112: 301–319
- Schumann U (1987) Influence of mesoscale orography on idealized cold fronts. *J Atmos Sci* 44: 3423–3441
- Scinocca JF, Peltier WR (1989) Pulsating downslope windstorms. *J Atmos Sci* 46: 2885–2914
- Scorer RS (1949) Theory of waves in the lee of mountains. *Quart J Roy Meteor Soc* 75: 41–56
- Siebert P (1990) South foehn studies since the ALPEX experiment. *Meteor Atmos Phys* 43: 91–103
- Smith RB (1985) On severe downslope winds. *J Atmos Sci* 43: 2597–2603
- Smith RB (1987) Aerial observations of the Yugoslavian bora. *J Atmos Sci* 44: 269–297
- Therry G, LaCarrère P (1983) Improving the eddy kinetic energy model for planetary boundary layer description. *Bound-Layer Meteor* 25: 63–88
- Volkert HL, Weickmann L, Tafferfer A (1991) The “Papal Front” of 3 May 1987 – A remarkable example of frontogenesis near the Alps. *Quart J Roy Meteor Soc* 117: 125–150
- Williams RT, Peng MS, Zankofski DA (1992) Effects of topography on fronts. *J Atmos Sci* 49: 287–305
- Zong JX, Xu Q (1997) The dynamics of cold fronts passing over a quasi-two-dimensional mountain ridge, *Tellus* 49: 559–576

Authors' addresses: James D. Doyle, Naval Research Laboratory, Marine Meteorology Division, 7 Grace Hopper Avenue, Monterey, CA 93943-5502 USA (E-Mail: doyle@nrlmry.navy.mil); M. A. Shapiro, National Center for Atmospheric Research/NOAA/ERL Environmental Technology Laboratory, Boulder, CO, 80301 USA